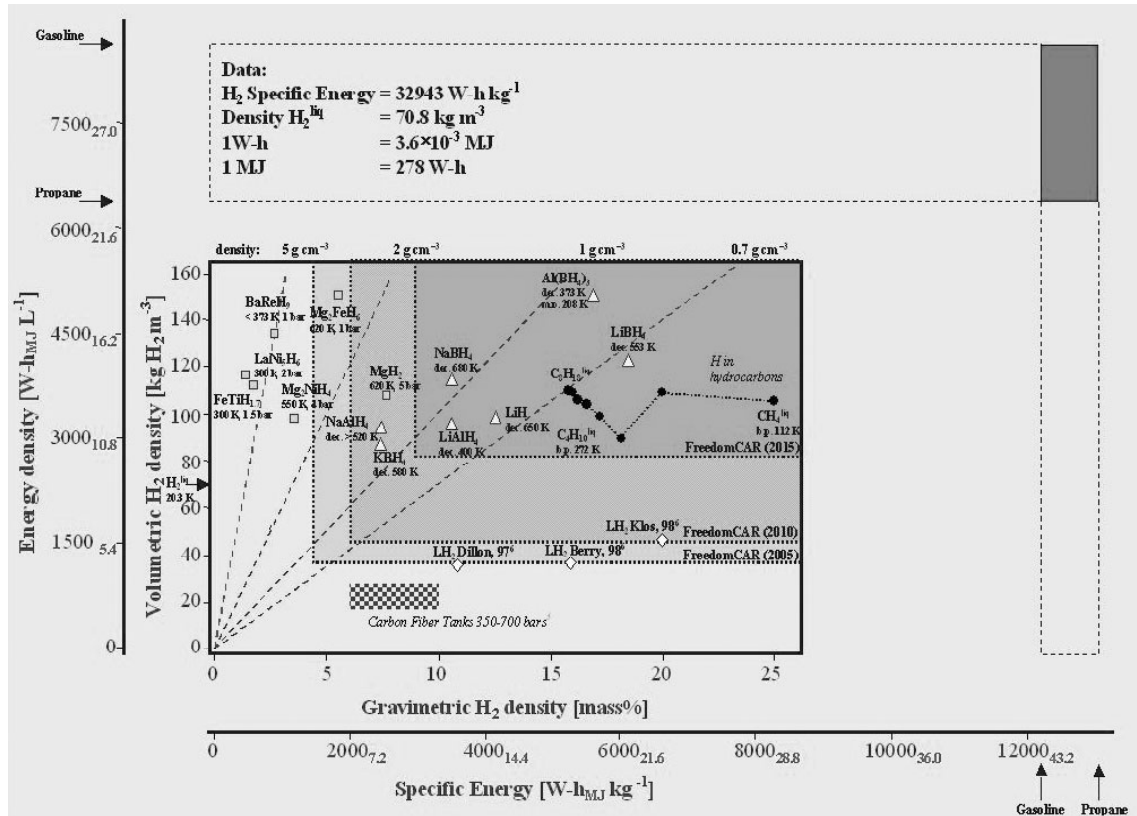


## Chapter 2: Literature Survey

In recent years, it has become increasingly clear that hydrogen as an energy carrier is ‘in’ and carbonaceous fuels are ‘out’. The hydrogen economy is coming, with the impetus to transform our fossil energy-based society, which inevitably will cease to exist, into a renewable energy-based one. However, this transformation will not occur overnight. It may take several decades to realize a hydrogen economy. In the meantime, research and development is necessary to ensure that the implementation of the hydrogen economy is completely seamless, with essentially no disruption of the day-to-day activities of the global economy. The world has taken on a monumental, but not insurmountable, task of transforming from carbonaceous to renewable fuels, with clean burning, carbon dioxide-free hydrogen as the logical choice.

One of the key roadblocks to the widespread use of hydrogen as a renewable fuel, especially on-board passenger vehicles, is hydrogen storage. Three options exist for storing hydrogen: as a highly compressed gas, a cryogenic liquid, or in a solid matrix. However, because hydrogen is the lightest element known, the gravimetric and volumetric densities of any storage system will necessarily be very low, especially compared to carbonaceous fuels. To put these storage options into perspective, Fig.2.1 compares the gravimetric and volumetric densities, and corresponding specific energies and energy densities, of a variety of different hydrogen storage media with two common fossil fuels, gasoline and propane.



**Figure 2.1** Gravimetric and volumetric densities, and corresponding specific energies and energy densities, of a variety of different hydrogen storage media, including two common fossil fuels, gasoline, and propane. The FreedomCar targets for 2005, 2010, and 2015 are indicated within the shaded regions. The gravimetric hydrogen densities for pressurized hydrogen gas and cryogenic liquid hydrogen (diamond symbols) include the mass of the storage container, whereas the values reported for the metal hydrides, complex hydrides, and other hydrogen storage materials are based on the absolute (theoretical) amount of hydrogen. [Ritter et al.]

For transportation, 4–6 kg of hydrogen needs to be stored in a mid-sized, fuel cell-powered vehicle for a range of 500 km. However at atmospheric pressure (1 atm) and ambient temperature (298 K), 5 kg of hydrogen occupies  $60 \text{ m}^3$ , a viable but not practical option for on-board vehicles. In contrast, 5 kg of gaseous hydrogen at ambient temperature in a 5000 psi composite tank, which is being commercialized for on-board vehicles, needs an internal volume of  $0.2 \text{ m}^3$ . This corresponds to four or five of these high-pressure tanks, a feasible but still not desirable option for on-board vehicles. Cryogenic hydrogen, with a liquid density of  $70.8 \text{ kg/m}^3$ , seems the best option from a volumetric point of view, as 5 kg occupies an internal volume of only  $0.07 \text{ m}^3$ . A

specially designed, super-insulated tank for cryogenic hydrogen is currently under commercialization Fig 2.2.



**Figure 2.2** A hydrogen storage tank for BMW ([www.bmw.com](http://www.bmw.com))

Most automakers are considering either the high-pressure gaseous or cryogenic liquid hydrogen storage options for passenger vehicles. However, these two technologies are fraught with public perception issues on safety. Other issues also need to be addressed, including compression costs and safety, liquefaction costs, and dormancy. Fig.2.1 shows that neither of these storage options meets the long-term needs of automakers and barely those in the near-term. For this reason, it is becoming increasingly accepted that the solid matrix method of hydrogen storage is the only option that has any hope of achieving the gravimetric and volumetric densities identified in Fig.2.1 for the FreedomCar goals.

There are essentially two ways to run a road vehicle on hydrogen. In the first, hydrogen in an internal combustion engine is burnt rapidly with oxygen from air. The efficiency of the transformation from chemical to mechanical through thermal energy is limited by the Carnot efficiency and is slightly higher for hydrogen–air mixtures (around 25%) than for petrol–air mixtures. When a lean mixture is used, the exhaust gas contains nothing but water vapour; richer mixtures also produce  $\text{NO}_x$ . In the second method, hydrogen is 'burnt' electrochemically with oxygen from air in a fuel cell, which

produces electricity (and heat) and drives an electric engine. Here, the efficiency of the direct process of electron transfer from oxygen to hydrogen is not limited by the Carnot efficiency; it can reach 50–60%, twice as much as the thermal process.

For on-board energy storage, vehicles need compact, light, safe and affordable containment. A modern, commercially available car optimized for mobility and not prestige with a range of 400 km burns about 24 kg of petrol in a combustion engine; to cover the same range, 8 kg hydrogen are needed for the combustion engine version or 4kg hydrogen for an electric car with a fuel cell.

Properties	Hydrogen (H <sub>2</sub> )	Methane (CH <sub>4</sub> )	Petrol (–CH <sub>2</sub> –)
Lower heating value (kWh kg <sup>-1</sup> )	33.33	13.9	12.4
Self-ignition temperature (°C)	585	540	228–501
Flame temperature (°C)	2,045	1875	2,200
Ignition limits in air (Vol%)	4–75	5.3–15	1.0–7.6
Minimal ignition energy (mW s)	0.02	0.29	0.24
Flame propagation in air (m s <sup>-1</sup> )	2.65	0.4	0.4
Diffusion coefficient in air (cm <sup>2</sup> s <sup>-1</sup> )	0.61	0.16	0.05
Toxicity	No	No	High

Hydrogen is a molecular gas. At room temperature and atmospheric pressure, 4 kg of hydrogen occupies a volume of 45 m<sup>3</sup>. This corresponds to a balloon of 5 m diameter, hardly a practical solution for a vehicle (Table2.1) [Schlapbach & Züttel, 2001] (Fig. 2.3) [Schlapbach & Züttel, 2001].

One of the 2010 technical targets of the US-DOE for on-board hydrogen storage is to overcome a “commercialization barrier” of about 6 wt.% hydrogen a storage material

should contain (Table 2.2). At the same time the density of the material should not be too low so that the volume of the tank stays in an acceptable range. The upper operating temperature of the storage is defined and limited by the working temperature of the PEM fuel cell (currently 80–100 °C).

**Table 2.2** Department of Energy(DOE) technical target: On-Board hydrogen storage system

Storage Parameter	Units	2007*	2010	2015
Usable, specific-energy from H <sub>2</sub> (net useful energy/max <i>system</i> mass) <sup>d</sup> (“Gravimetric Capacity”)	kWh/kg (wt.% hydrogen)	1.5 (4.5%)	2 (6%)	3 (9%)
Usable energy density from H <sub>2</sub> (net useful energy/max <i>system</i> volume) (“Volumetric Capacity”)	kWh/L (kg H <sub>2</sub> /L)	1.2 (0.036)	1.5 (0.045)	2.7 (0.081)
Storage system cost <sup>e</sup>	\$/kWh net (\$/kg H <sub>2</sub> )	6 (200)	4 (133)	2 (67)
Fuel cost <sup>f</sup>	\$/per gallon gasoline equivalent at pump	3	1.5*	1.5*
Operating ambient temperature <sup>g</sup>	°C	-20/50 (sun)	-30/50 (sun)	-40/60 (sun)
Cycle life (1/4 tank to full) <sup>h</sup>	Cycles	500	1000	1500
Cycle life variation <sup>i</sup>	% of mean (min) @ % confidence	N/A	90/90	99/90
Minimum and Maximum delivery temperature of H <sub>2</sub> from tank	°C	-20/85	-30/85	-40/85
Minimum full-flow rate	(g/s)/kW	0.02	0.02	0.02
Minimum delivery pressure of H <sub>2</sub> from tank; FC=fuel cell, I=ICE	Atm (abs)	8 FC 10 ICE	4 FC 35 ICE	3 FC 35 ICE
Maximum delivery pressure of H <sub>2</sub> from tank <sup>j</sup>	Atm (abs)	100	100	100
Transient response 10%-90% and 9%-0% <sup>k</sup>	s	1.75	0.75	0.5
Start time to full-flow at 20°C <sup>l</sup>	s	4	4	0.5
Start time to full-flow at minimum ambient <sup>m</sup>	s	8	8	2
System Fill Time for 5-kg hydrogen	min	10	3	2.5
Loss of useable hydrogen <sup>n</sup>	(g/h)/kg H <sub>2</sub> stored	1	0.1	0.05
Permeation and leakage <sup>o</sup>	Sc/h	Federal enclosed-area safety-standard		
Toxicity		Meets or exceeds applicable standards		
Safety		Meets or exceeds applicable standards		
Purity <sup>p</sup> (H <sub>2</sub> from storage system)		98% (dry basis)		



**Figure 2.3** Volume of 4 kg of hydrogen compacted in different ways, with size relative to the size of a car. [Schlapbach & Züttel, 2001]

## 2.1 Hydrogen

Hydrogen is the lightest and most abundant element in the universe. It is an energy carrier, not an energy source, meaning that it stores and delivers energy in a usable form. In its pure form ( $H_2$ ), it is a colourless and odourless gas. However, since it combines easily with other elements, hydrogen is rarely found by itself in nature and is usually found as a part of other compounds, including fossil fuels, plant material, and water.

### 2.1.1 Hydrogen Properties

Hydrogen is a colourless, odourless, tasteless, and non-poisonous gas under normal conditions on Earth. It typically exists as a diatomic molecule, meaning each molecule has two atoms of hydrogen; this is why pure hydrogen is commonly expressed as " $H_2$ ". Hydrogen is the most abundant element in the universe, accounting for 90 percent of the universe by weight. However, it is not commonly found in its pure form, since it readily

combines with other elements. It is also the lightest element, having a density of 0.08988 grams per liter at standard pressure.

Hydrogen has several important chemical properties that affect its use as a fuel:

- It readily combines with oxygen to form water, which is absolutely necessary for life on this planet.
- It has high energy content per weight (nearly 3 times as much as gasoline), but the energy density per volume is quite low at standard temperature and pressure. Storing the hydrogen under increased pressure or storing it at extremely low temperatures as a liquid can increase volumetric energy density. Hydrogen can also be adsorbed into metal hydrides.
- Hydrogen is highly flammable; it only takes a small amount of energy to ignite it and make it burn. It also has a wide flammability range, meaning it can burn when it makes up 4 to 74 percent of the air by volume.
- Hydrogen burns with a pale-blue, almost-invisible flame, making hydrogen fires difficult to see.
- The combustion of hydrogen does not produce carbon dioxide (CO<sub>2</sub>), particulate, or sulphur emissions. It can produce nitrous oxide (NO<sub>x</sub>) emissions under some conditions.
- Hydrogen can be produced from renewable resources, such as by reforming ethanol (this process emits some carbon dioxide) and by the electrolysis of water (electrolysis is very expensive).

### 2.1.2 Hydrogen Production

Hydrogen can be produced using a variety of domestic energy resources - fossil fuels, such as coal and natural gas, with carbon capture and sequestration; renewable, such as biomass, and renewable energy technologies, including solar, wind, geothermal, and hydropower; and nuclear power. Specific technologies and processes are described below.

#### 2.1.2.1 Thermochemical Processes

**Steam methane reforming:** In this process, high-temperature steam is used to extract hydrogen from a methane source such as natural gas. This is the most common method of producing hydrogen.

**Partial oxidation:** Scientists are exploring a process that produces hydrogen by simultaneously separating oxygen from air and partially oxidizing methane.

**Other thermal processes:** Other processes include splitting water, using heat from a solar concentrator, and gasifying or burning biomass (i.e., biological material, such as plants or agricultural waste) to generate a bio-oil or gas, which is then reformed to produce hydrogen.

#### 2.1.2.2 Electrolytic Processes

**Electrolysis:** In electrolysis, electricity is used to separate water (H<sub>2</sub>O) into hydrogen and oxygen. Current electrolysis systems are very energy intensive. The challenge is to develop low cost and more energy efficient electrolysis technologies.

### 2.1.2.3 Photolytic Processes

**Photolytic methods:** In photolysis, sunlight is used to split water. Photolytic processes are:

- 1) Photobiological methods, in which microbes, when exposed to sunlight, split water to produce hydrogen
- 2) Photoelectrolysis, in which semi-conductors, when exposed to sunlight and submersed in water, generate enough electricity to produce hydrogen by splitting the water.

### 2.1.3 Potential Applications

Hydrogen can be used in fuel cells to power a wide variety of applications, both mobile and stationary, small- and large-scale. Fuel cells can be used to provide clean energy for transportation. And because they are modular, fuel cells can provide heat and electricity for single homes or to supply the energy to run an entire large commercial building, to provide a small amount of electricity to a community grid, or a large amount of electricity to a large grid network.

Hydrogen can be used to generate electricity for our homes and office buildings, through the use of gas turbines and microturbines (small gas turbines). Conventional gas

turbines can be modified to run efficiently on hydrogen or hydrogen/natural gas blends. Microturbines can provide high-efficiency reliable power for smaller-scale applications.

Hydrogen can also be used in internal combustion engines for both stationary and mobile applications, powering industrial processes, ocean fleets, cars, and buses. As with gas turbines, conventional combustion engines can be modified to run efficiently on hydrogen or hydrogen/natural gas mixtures for these applications.

## **2.2 Gaseous and Liquid Hydrogen Storage**

Today's state-of-the-art for hydrogen storage includes 5000- and 10,000-psi compressed gas tanks and cryogenic liquid hydrogen tanks for on-board hydrogen storage.

### **2.2.1 Compressed Hydrogen Gas Tanks**

The energy density of gaseous hydrogen can be improved by storing hydrogen at higher pressures. This requires material and design improvements in order to ensure tank integrity. Advances in compression technologies are also required to improve efficiencies and reduce the cost of producing high-pressure hydrogen.

Carbon fiber-reinforced 5000-psi and 10,000-psi compressed hydrogen gas tanks are under development by Quantum Technologies and others Fig. 2.2.1. Such tanks are already in use in prototype hydrogen-powered vehicles. The inner liner of the tank is a high molecular weight polymer that serves as a hydrogen gas permeation barrier. A carbon fiber-epoxy resin composite shell is placed over the liner and constitutes the gas

pressure load-bearing component of the tank. Finally, an outer shell is placed on the tank for impact and damage resistance. The pressure regulator for the 10,000-psi tank is located in the interior of the tank. There is also an in-tank gas temperature sensor to monitor the tank temperature during the gas filling process when heating of the tank occurs.



**Figure 2.2.1** Tucked inside the trunk of the Ford Focus is a gas tank with the capacity for holding enough hydrogen to go 200 miles. [Credit: NASA]

The driving range of fuel cell vehicles with compressed hydrogen tanks depends, of course, on vehicle type, design and the amount and pressure of stored hydrogen. By increasing the amount and pressure of hydrogen, a greater driving range can be achieved but at the expense of cost and valuable space within the vehicle. Volumetric capacity, high pressure and cost are thus key challenges for compressed hydrogen tanks. Refueling times, compression energy penalties and heat management requirements during compression also need to be considered as the mass and pressure of on-board hydrogen are increased.

Issues with compressed hydrogen gas tanks revolve around high pressure, weight, volume, conformability and cost. The cost of high-pressure compressed gas tanks is essentially dictated by the cost of the carbon fiber that must be used for lightweight structural reinforcement. Efforts are underway to identify lower-cost carbon fiber that

can meet the required high pressure and safety specifications for hydrogen gas tanks. However, lower-cost carbon fibers must still be capable of meeting tank thickness constraints in order to help meet volumetric capacity targets. Thus lowering cost without compromising weight and volume is a key challenge.

### 2.2.2 Liquid Hydrogen Tanks

The energy density of hydrogen can be improved by storing hydrogen in a liquid state. However, the issues with LH2 tanks are hydrogen boil-off, the energy required for hydrogen liquefaction, volume, weight, and tank cost. The energy requirement for hydrogen liquefaction is high; typically 30% of the heating value of hydrogen is required for liquefaction. New approaches that can lower these energy requirements and thus the cost of liquefaction are needed. Hydrogen boil-off must be minimized or eliminated for cost, efficiency and vehicle range considerations, as well as for safety considerations when vehicles are parked in confined spaces. Insulation is required for LH2 tanks and this reduces system gravimetric and volumetric capacity.

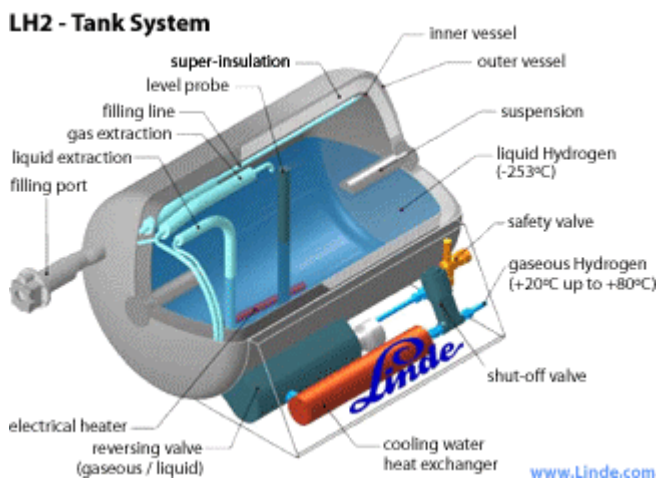


**Figure 2.2.2** Liquid hydrogen (LH2) tanks

Liquid hydrogen (LH<sub>2</sub>) tanks (Fig. 2.2.2) can store more hydrogen in a given volume than compressed gas tanks. The volumetric capacity of liquid hydrogen is 0.070 kg/L, compared to 0.030 kg/L for 10,000 psi gas tanks.

Liquid tanks are being demonstrated in hydrogen-powered vehicles and a hybrid tank concept combining both high-pressure gaseous and cryogenic storage is being studied. These hybrid (cryo-compressed tanks) insulated pressure vessels are lighter than hydrides and more compact than ambient-temperature, high pressure vessels. Because the temperatures required are not as low as for liquid hydrogen, there is less of an energy penalty for liquefaction and less evaporative losses than for liquid hydrogen tanks.

### **2.3 Metal Hydrides**

Metal hydrides are a promising means of efficiently storing hydrogen due to their high storage capabilities at low pressure, whilst they also maintaining volumetric densities comparable to that of liquid hydrogen. The highest volumetric densities of hydrogen on any material are found in metal hydrides (Fig. 2.1), which are defined as a concentrated single phase compounds involving the host metal and hydrogen.

Hydrides can broadly classified as Follows:

- 1) Ionic hydrides in which hydrogen exist as H<sup>-</sup> e.g. MH, M is mainly alkali or alkaline earth metal.

- 2) Covalent hydrides in which hydrogen shares the electron pair with non-metals or atoms with similar electro negativities e.g. H<sub>2</sub>O, H<sub>2</sub>S, SiH<sub>4</sub>, hydrocarbons, etc.
- 3) Metal Hydrides in which hydrogen act as a metal and are mainly formed with transition metals including the rare earth and actinide series.

Metal hydrides containing one metal have limited practical applications in hydrogen storage because of the high thermodynamic stability of these compounds. For this reason, a wide range of alloys with two or more metals have been investigated over the past several decades in order to find a material that meets the practical requirements. Metallic hydrides form a wide range of stoichiometric and non-stoichiometric compounds with direct interaction of hydrogen with metals. The hydrogen atoms enter the metal lattice to form a solid solution and metal hydrides begin to crystallize when the local hydrogen concentration exceeds a certain limit. The rate of entry and reaction depends in part on the metal particle size, and for this reason more efficient hydrogen sorption capabilities can be achieved with nanosized metals as compared to their bulk counterparts. These alloys show more complex thermodynamics and phase diagrams than the pure metal hydrides, and may therefore lead to a material with commercial hydrogen storage applications.

A range of nanocrystalline metal hydrides can be prepared by mechanochemical process such as high-energy ball milling. This technique provides easy preparation of samples, flexible grain size control, as well as easy scale-up, and the nanosized metal hydrides thus-formed show higher hydrogen sorption capacities compared to the bulk hydride material. Once ball-milled, some metal hydrides and intermetallic compounds need to be activated due to a thin oxide layer formed during milling, and the first cycle of

hydrogenation and dehydrogenation should be performed under relatively high pressure. The hydrogen sorption kinetics was found to be increased by ball milling in the presence of certain organic additives, this method is called doping.

From recent research by scientists it is apparent that the main disadvantage of metal hydrides, even in their nanocrystalline form, are their low gravimetric hydrogen content, the high temperature needed for desorption of hydrogen, and problem associated with their regeneration. Other problems associated with their use indicate the cost, low specific uptake by weight in many cases, unfavourable kinetics requiring heating cycle, and susceptibility to contamination by impurities.

## 2.4 Complex Hydrides

Complex hydrides are inorganic salt like compounds of anion such as  $[\text{BH}_4]^-$ ,  $[\text{AlH}_4]^-$ , stabilized mainly light metal cations. The hydrogen in the complex hydride is located at the corners of a tetrahedron with the metal in the centre, and the negative charge of the anion,  $[\text{BH}_4]^-$  and  $[\text{AlH}_4]^-$ , is compensated by a cation, such as Li or Na. The hydride complexes of boron, the tetrahydroborate  $\text{M}(\text{BH}_4)$ , and of aluminium, the tetrahydroaluminate  $\text{M}(\text{AlH}_4)$ , are perhaps the most promising hydrogen-storage material discovered to date, as they have shown promising level of reversible adsorption according to the DOE targets of 6 wt.%. In their pure bulk form they are thermodynamically quite stable and decompose only at elevated temperatures, often above the melting point. However, decomposition temperature can be reduced and the hydrogen adsorption efficiency improved by using various dopants or reducing the grain size. Some of the common complex hydrides and their wt.% hydrogen storage capacity

is listed in Table 2. This is from the US-DOE report, in which these complex hydrides are considered for hydrogen storage.

**Table 2.3.1** Available Hydrogen in Select Complex Hydrides [FY 2002].

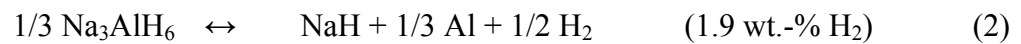
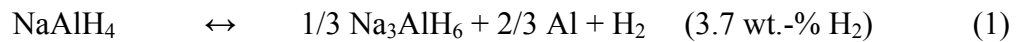
Complex Hydride	Wt %
$\text{LiAlH}_4$	10.5
$\text{LiBH}_4$	18.2
$\text{Al}(\text{BH}_4)_3$	20.0
$\text{LiAlH}_2(\text{BH}_4)_2$	15.2
$\text{Mg}(\text{AlH}_4)_2$	9.3
$\text{Mg}(\text{BH}_4)_2$	14.8
$\text{Ca}(\text{AlH}_4)_2$	7.7
$\text{Ca}(\text{BH}_4)_2$	11.4
$\text{NaAlH}_4$	7.5
$\text{NaBH}_4$	10.5
$\text{Ti}(\text{BH}_4)_3$	12.9
$\text{Ti}(\text{AlH}_4)_4$	9.3
$\text{Zr}(\text{BH}_4)_3$	8.8
$\text{Fe}(\text{BH}_4)_3$	11.9

#### 2.4.1. Aluminium Hydride (Alanate)

Aluminium hydride is one of the materials that have shown potential for hydrogen storage. This is because it contains high weight percentage of hydrogen, much of which can be removed and replaced continuously. One drawback of aluminium hydrides is that they are not always easy to prepare. However, Huot et al, have shown that  $\text{Na}_3\text{AlH}_6$  and  $\text{Na}_2\text{LiAlH}_6$  can easily be produced by energetic ball-milling of NaH, LiH and NaAlH<sub>4</sub> in stoichiometric composition. No high temperature, high pressure or purification steps

are needed. In the case of  $\text{Na}_3\text{AlH}_6$ , the metastable high temperature  $\beta\text{-Na}_3\text{AlH}_6$  is formed, along with some  $\alpha\text{-Na}_3\text{AlH}_6$ . Energetic ball-milling of stoichiometric mixtures of  $\text{NaAlH}_4$ ,  $\text{NaH}$  and  $\text{LiH}$  produced  $\text{Na}_2\text{LiAlH}_6$ .

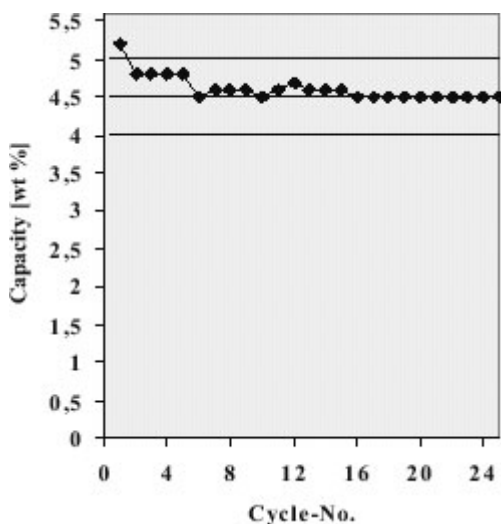
The mechanism and dynamics of hydrogen desorption have been extensively studied. Thermal decomposition of  $\text{NaAlH}_4$  at high temperature takes place in two steps to give  $\text{NaH}$ ,  $\text{Al}$ , and  $\text{H}_2$ . In principle the first step can give 3.7 wt.-%  $\text{H}_2$ , and up to 5.6 wt.-% in the second step:



In step 1,  $\text{NaAlH}_4$  decomposes to  $\text{Na}_3\text{AlH}_6$ , followed by decomposition to  $\text{NaH}$  in step 2. Due to its high binding energy,  $\text{NaH}$  is not applicable for a reversible hydrogen source. Before the decomposition of  $\text{NaH}$ , theoretically 5.6 wt.% of hydrogen is reversibly discharged from  $\text{NaAlH}_4$ . The first two steps of decomposition can be substantially reduced by doping with other metal cations such as  $\text{Ti}^{3+}$ ,  $\text{Ti}^{4+}$ ,  $\text{Zr}^{4+}$ ,  $\text{Fe}^{+3}$ , etc [Bogdanovic et al., 2003 a].

Recently Bogdanovic et al. [2003 b] reported that doping Na alanate with  $\text{TiN}$  nanoparticles could substantially reduce the temperature required for deposition as well as the hydrogenation time required time for practical purposes, and the desorbs hydrogen can reach close to the theoretical limit. However the hydrogen capacity for

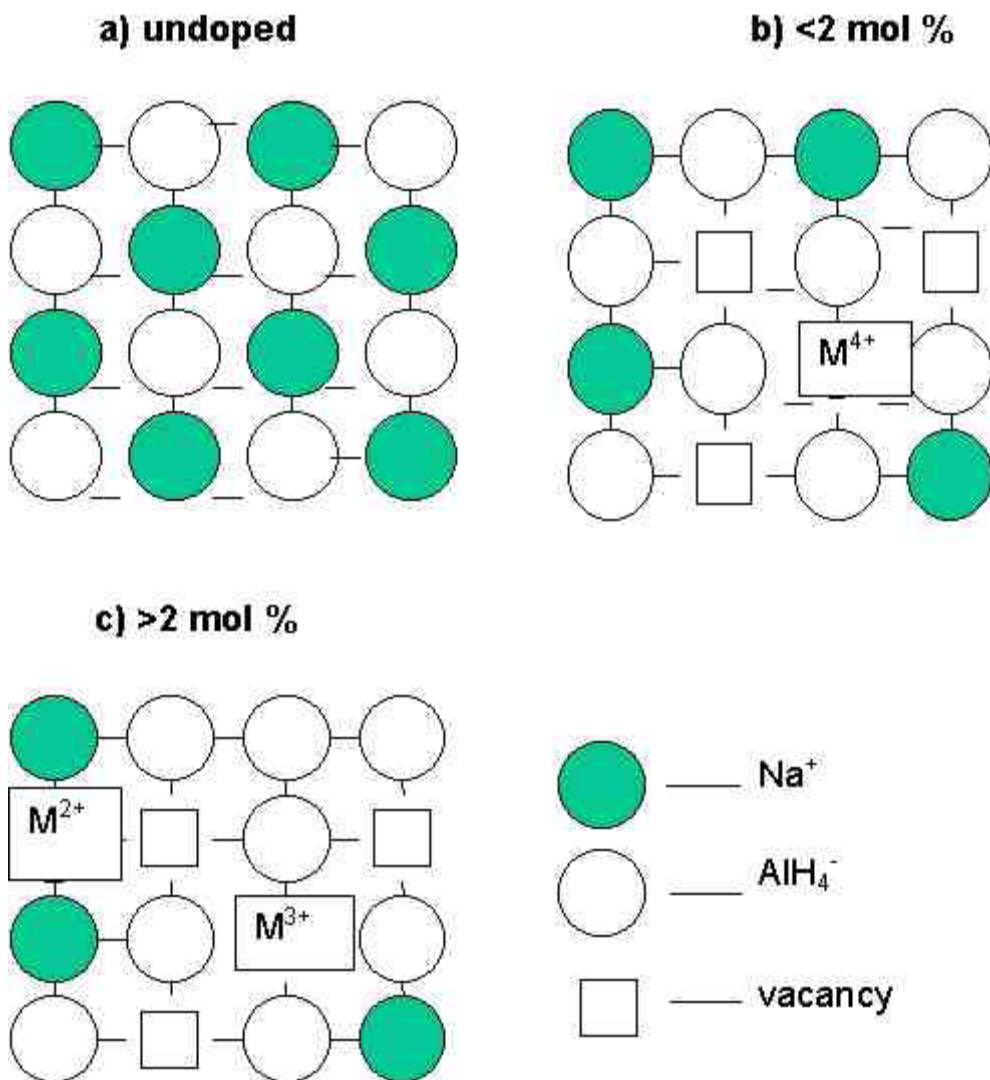
these materials is found to be slightly decreased over the course of several cycles before stabilizing (Fig. 2.4.1.1).



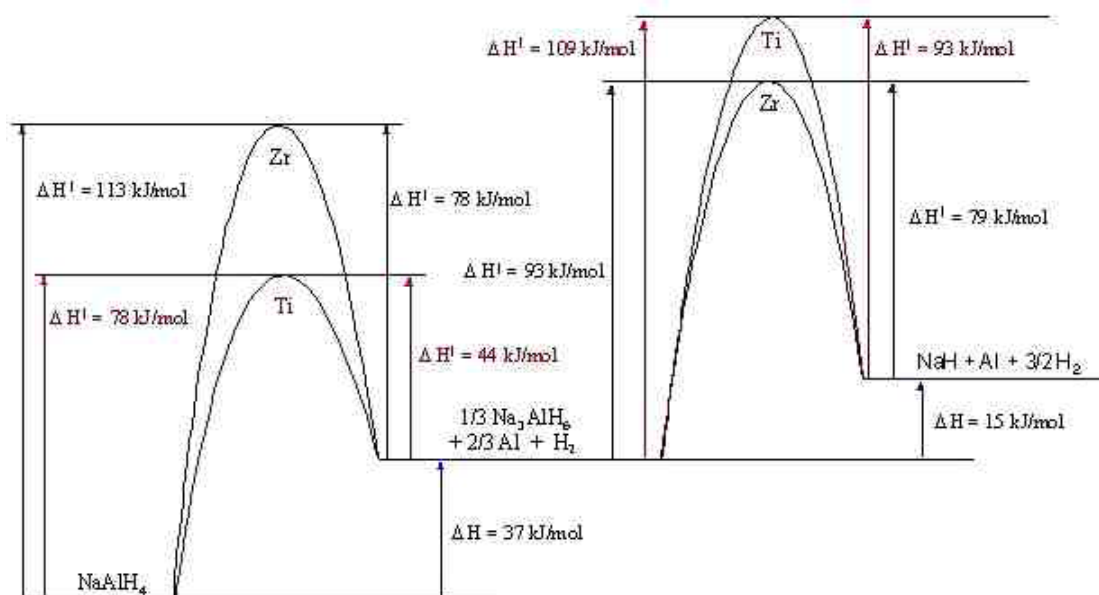
**Figure 2.4.1.1** Hydrogen-storage capacity level in 25 cycle test of NaAlH<sub>4</sub> doped with 2 mol.% TiN nanoparticles. Dehydrogenation at 120/180 °C and normal pressure; hydrogenation at 100 °C and 100-85 bar pressure. [Bogdanovic et al., 2003]

Jensen et al. studies of doped NaAlH<sub>4</sub> have given important insights into the highly promising but enigmatic hydrogen storage properties of this material. Their kinetic studies strongly suggest that the rate of the dehydrogenation and hydrogenation reactions are limited by the micro-reverse of the fundamental Al-H bond breaking process. Their X-ray diffraction and solid-state NMR studies have shown that doping results in bulk changes to the crystal lattice of the hydride rather than the generation of surface isolated catalytic sites Fig. 2.4.1.3. This structural augmentation of the hydride affects bulk perturbation and mobilization of hydrogen. These observations that bulk structural changes occur upon doping the hydride have led us to develop a new model of the doped hydride which accounts for the structural changes as the result of substitution of Na<sup>+</sup> ions by M4<sup>+</sup> and M3<sup>+</sup> ions as shown in Fig. 2.4.1.4. In support of this “Na<sup>+</sup> substitution” model, the presence of Ti3<sup>+</sup> in samples NaAlH<sub>4</sub> that were doped with a

variety of titanium precursors has been confirmed through electron spin resonance studies.



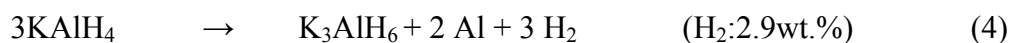
**Figure 2.4.1.2** Schematic Illustration of the Changes in the  $\text{NaAlH}_4$  Lattice upon Increased Level of Doping (a) Undoped hydride; (b) Substitution of  $\text{Na}^+$  by  $\text{M}^{4+}$  and requisite formation of 3  $\text{Na}^+$  vacancies upon doping with 2 mol %  $\text{M}^{4+}$ ; (c) increasing substitution without increasing  $\text{Na}^+$  vacancies requires  $\text{M}$  to be present as  $\text{M}^{3+}$  or  $\text{M}^{2+}$  at higher doping levels. [Jensen et al., FY 2002]

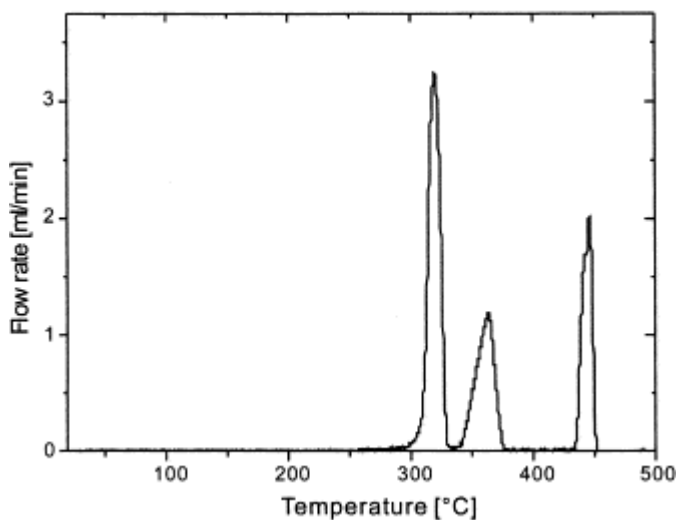


**Figure 2.4.1.3** Energy-Reaction Profile for the Reversible Dehydrogenation of NaAlH<sub>4</sub> to NaH + Al [Jensen et al., FY 2002]

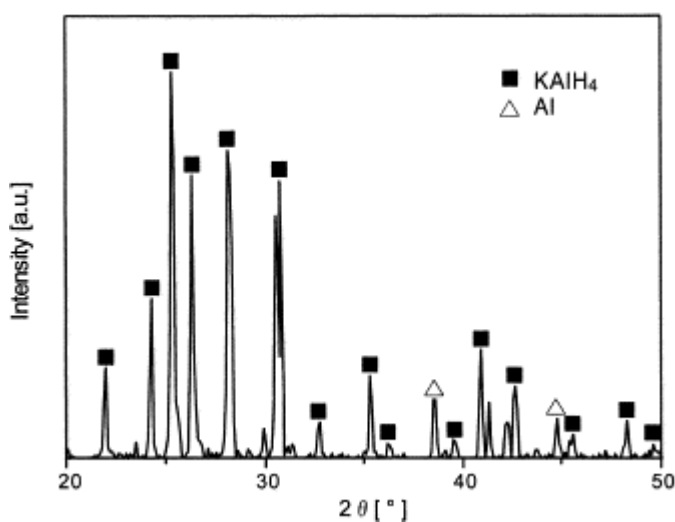
Morioka et al. have worked on KAlH<sub>4</sub> and demonstrated the reversible hydrogen desorption. The hydrogen ability was above 3.5 wt.% under 10 bar of hydrogen in a temperature range of 250–330 °C, the reversible reaction smoothly proceeds without any catalyst, which is different from the reactions of NaAlH<sub>4</sub> and LiAlH<sub>4</sub>, in which homogeneous doping of a transition metal catalyst is essential for reversibility and good kinetics. These findings provide new guidelines for a systematic understanding of the reversible hydrogen decomposition of the alanate family.

Fig. 2.4.1.4 shows the dehydrogenation behavior of KAlH<sub>4</sub>. The expected decomposition processes are as in (4), (5) and (6), in analogy with the decomposition process of NaAlH<sub>4</sub>.





**Figure 2.4.1.4** TPD measurement of  $\text{KAlH}_4$  dehydrogenation. The sample was heated from room temperature to 500 °C at the rate of 2 °C/min. Please refer to(4), (5), and (6) for the decomposition reaction. [Morioka et al., 2003]



**Figure 2.4.1.5** X-ray powder diffraction measurement of  $\text{KAlH}_4$ , synthesized from  $\text{KH}$  and  $\text{Al}$  at 270 °C at >175 bar of hydrogen (reaction7). [Morioka et al., 2003]



Fig.2.4.5 shows the result of X-ray diffraction measurement of the synthesized compound indicating that  $\text{KAlH}_4$  was formed by reaction (7), though a small amount of unreacted residual aluminum was included.

The first dehydrogenation occurred at approximately 300 °C to decompose to  $K_3AlH_6$  and Al (reaction (4)), and 2.4 wt.% of hydrogen was released, which is comparable to its theoretical value of 2.9 wt.%. The second and third dehydrogenation steps, (5) and (6), occurred approximately at 340 and 430 °C, respectively, and 1.3 and 1.2 wt.% of hydrogen was released. These values agree reasonably well with the theoretical values, 1.4 wt.% for both steps. It seems, therefore, that the decompositions followed (4), (5) and (6), and the initial content of  $KAlH_4$  in the sample was more than 80%.

### 2.2.2. Borohydride (Borate)

Borohydride are a promising group of compounds for hydrogen storage. As from the Table 2.4.4.1 it is quite clear that Borohydride are the material that have the highest hydrogen storage capacity. The hydrogen content can reach the value of up to 20 wt.% for  $BH_4$ . Züttel et al. have worked quite extensively on  $LiBH_4$  and according to them, the structure of  $LiBH_4$  is orthorhombic. The unit cell contains four molecules and has the dimensions  $a=7.1730 \text{ \AA}$ ,  $b=4.4340 \text{ \AA}$ ,  $c=6.7976 \text{ \AA}$  at 25 °C (Fig. 2.4.1.6). The calculated density of  $LiBH_4$  is  $0.669 \text{ g cm}^{-3}$ . Each  $Li^+$ -ion is surrounded by four  $[BH_4]^-$  ions in a tetrahedral configuration. The  $[BH_4]$  tetrahedrons are strongly deformed, two hydrogen atoms are at a bond length of  $d(B---H)=1.30 \text{ \AA}$ , one at  $d(B---H)=1.28 \text{ \AA}$  and one at  $d(B---H)=1.44 \text{ \AA}$ .

Pistorius investigated the phase diagram of  $LiBH_4$  over a large temperature and pressure range and found a structural transition from the orthorhombic phase at low temperature to a tetragonal phase around 105 °C. However, the structural transition around 100 °C is accompanied by a hydrogen desorption and therefore not only the structure but also the

composition changes slightly. The thermal desorption spectra of pure  $\text{LiBH}_4$  shown in Fig. 4.4.2.2a exhibits a slight hydrogen desorption between 100 and 200 °C of 0.3 mass% or approximately 1.5% of the total hydrogen content of the compound which is in good agreement with the observation of Fedneva et al. The fusion was observed around 270 °C without liberation of hydrogen. At 320 °C the first significant hydrogen desorption peak starts and liberates an additional 1 mass% of hydrogen. This first desorption goes over to a second desorption peak starting at 400 °C and reaches its maximum around 500 °C. The integrated amount of hydrogen desorbed up to a temperature of 600 °C is 9 mass%, which corresponds exactly to half of the hydrogen in the starting compound. The end product has the nominal composition " $\text{LiBH}_2$ ". The thermal desorption spectra of  $\text{LiBH}_4$  mixed with  $\text{SiO}_2$ -powder (25:75 mass%) shown in 4.4.2.2b exhibits also three hydrogen desorption features, however the desorption starts at lower temperatures and 9 mass% of hydrogen are liberated below 400 °C. The first hydrogen desorption peak starts already at 200 °C and the second hydrogen desorption peak starts at 453 °C and is very sharp. The  $\text{SiO}_2$ -powder catalyzes the decomposition reaction of  $\text{LiBH}_4$  and lowers the temperature for all three hydrogen desorption features. Furthermore, the pure  $\text{LiBH}_4$  sample only exhibits significant desorption above 400 °C in the second hydrogen desorption peak while the first hydrogen desorption peak starting at 200 °C is the dominant peak of the catalyzed sample.

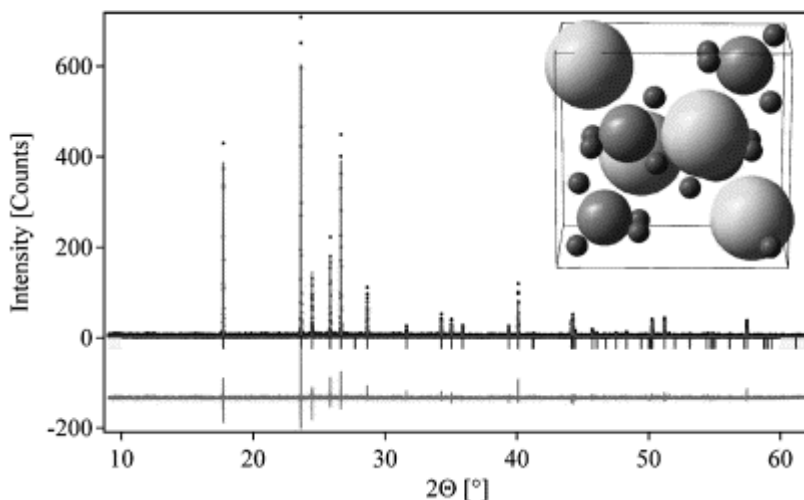


**Figure 2.4.2.1** Synchrotron powder diffraction spectrum (Debye–Scherrer) of polycrystalline  $\text{LiBH}_4$ . Space group  $Pnma$  (#62),  $a=7.1730(1)$  Å,  $b=4.4340(1)$  Å,  $c=6.7976(1)$  Å,  $V=216.20$  Å<sup>3</sup>,  $Z=4$ ,  $\rho = 0.669(2)$  g cm<sup>-3</sup>,  $R_{\text{Bragg}}=6.94\%$ ,  $R_{\text{wp}}=7.68\%$  and  $\chi^2=0.58$ . The inset shows a drawing of the orthorhombic unit cell containing four  $\text{LiBH}_4$ , the size of the atoms corresponds to 25% of their covalent radii. [Züttel et al. 2003]

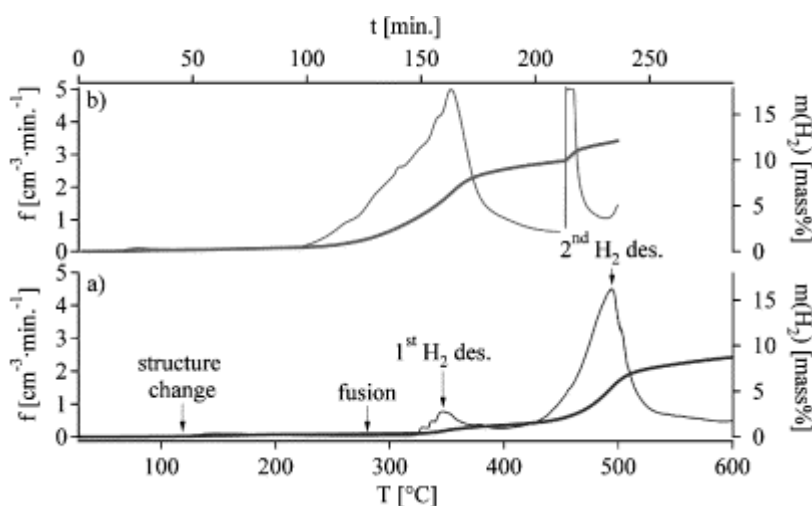
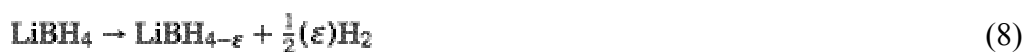


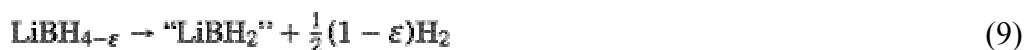
**Figure 2.4.2.2** Thermal desorption spectra of  $\text{LiBH}_4$ . The sample was heated after evacuation at room temperature with a heating rate of  $2 \text{ K min}^{-1}$ . The gas flow was measured as a function of time and the desorbed hydrogen was computed from the integrated gas flow: (a) pure  $\text{LiBH}_4$  and (b)  $\text{LiBH}_4$  mixed with  $\text{SiO}_2$  as catalystr. [Züttel et al. 2003]

The decomposition reaction of the catalyzed  $\text{LiBH}_4$  can be schematically described as follows:

1. Structural transition at  $T=108\text{ }^{\circ}\text{C}$ :



2. First hydrogen peak starting at  $T=200\text{ }^{\circ}\text{C}$ :



3. Second hydrogen peak starting at  $T=453\text{ }^{\circ}\text{C}$ :



The compound  $\text{LiBH}_2$  is in quotes, since such a compound is not known yet. However, the desorption of 9 mass% indicates such a composition. Furthermore, Fedneva et al. observed an endothermic effect at the composition "LiBH<sub>2</sub>". Thermal desorption spectroscopy with different heating rates was applied in order to determine the activation energy of the slight hydrogen desorption process around 100 °C. The logarithm of the ratio of the heating rate divided by the square of the peak temperature is a linear function of the inverse temperature if the hydrogen desorption is a first order reaction. The computed activation energy for the decomposition of  $\text{LiBH}_4$  around 100 °C is  $E_A=156\pm 20\text{ kJ mol}^{-1}$ .

The temperature of the major hydrogen desorption peaks strongly depends on the heating rate as shown in Fig. 10. At a small heating rate of 0.5 and 1 K min<sup>-1</sup> three distinct desorption peaks were observed. The peak maxima correspond to 0.33, 1.0 and 2.0 mol H per mol of  $\text{LiBH}_4$ . This indicates that the hydrogen desorption reaction is divided in at least three steps with intermediate products. The maximum amount of

desorbed hydrogen is limited to 13.5 mass% due to the formation of lithium hydride (LiH) which is stable up to 900 °C.

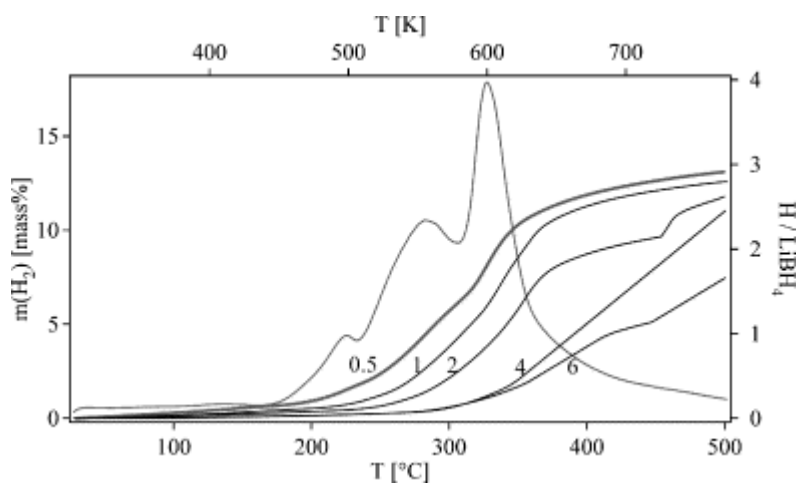


**Figure 2.4.2.3** Desorbed amount of hydrogen as a function of temperature for various heating rates, numbers indicate the heating rate in  $\text{K min}^{-1}$  on bottom and the hydrogen desorption flow as a function of temperature for a heating rate of  $0.5 \text{ K min}^{-1}$  on top. The sample was  $\text{LiBH}_4$  (28 mass%) mixed with  $\text{SiO}_2$ -powder. [Züttel et al. 2003]

Solids and nanocrystalline borohydrides of sodium and potassium are less explored, but molecularly dispersed aqueous Borohydride solution is a safe method for liberating hydrogen in a controllable way presents an alternative method to the use of solid-phase system. The spontaneous hydrolysis of Borohydride in aqueous solution can effectively liberate hydrogen in the presence of catalyst such as Ru and Ni. In principal, aqueous  $\text{NABH}_4$  solution can liberate 7.3 wt.% hydrogen and up to 6.5 wt.% hydrogen liberation is achieved at only 40 °C by using 10 wt.%  $\text{NaOH}$  solution. Generating hydrogen from alkaline  $\text{NABH}_4$  solutions in this way has many attractive advantages, such as:

1.  $\text{NABH}_4$  Solutions are non-flammable and stable in air for months.
2.  $\text{H}^2$  generation only occurs in the presence of selected catalysts and can even occur at 0 °C.

3. The only other product in the gas stream is water vapor and other products can be recycled.
4.  $H^2$  generation rates are easily controlled.
5. Volumetric and gravimetric  $H^2$  storage efficiencies are high.

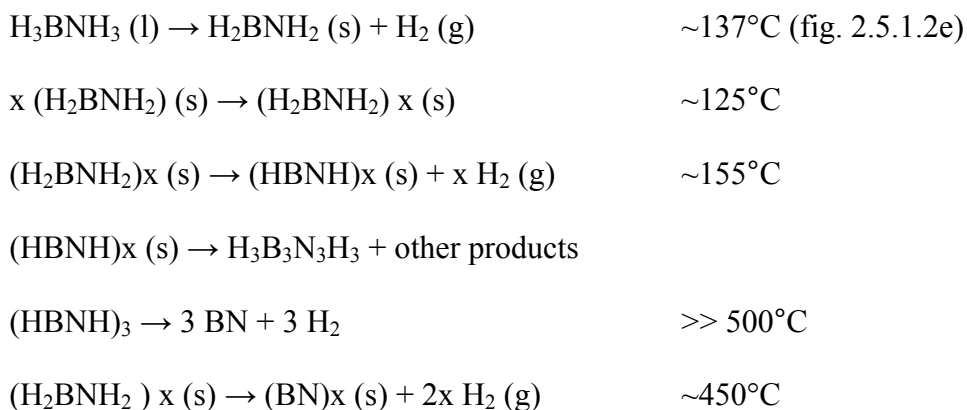
These points demonstrate that aqueous alkaline Borohydride is promising from a commercial standpoint in situations calling for a high-density source of hydrogen. While the generation of hydrogen from  $NABH_4$  is not reversible and lead to borate waste material, it is an excellent choice for one time application due to its high volumetric hydrogen content, which is greater than compressed hydrogen in gas cylinders.

### 2.5 Borazane ( $H_3BNH_3$ )

Physicochemical Properties of Borazane also called ammonia borazane ( $H_3BNH_3$ )

Formula	$H_3BNH_3$
Molecular weight	30.86
Odour	Ammonia-like
Density, g/ml	0.74
Melting point	112-114°C, slow decompose at approx. 70°C
Heat of formation	$DH_f^\circ = -42.54 \pm 1.4$ kcal/mol
Heat of combustion	$DH_c^\circ = -322.4 \pm 0.7$ kcal/mol

Pyrolysis of  $H_3BNH_3$  [Geanangel et al. (1985 and 1987)]



Borazane ( $\text{BH}_3\text{NH}_3$ ) is at ambient temperature and atmospheric pressure a white crystalline solid with relatively high hydrogen content (about 20 mass%  $\text{H}_2$ ). It is well known that borazane decomposes thermally activated already at temperatures below 410K. The decomposition takes place under hydrogen release and formation of aminoborane  $\text{BH}_2\text{NH}_2$  and borazine  $\text{B}_3\text{N}_3\text{H}_6$  according to the reaction equations in Fig.2.5.1 [Wolf et al., 2000].

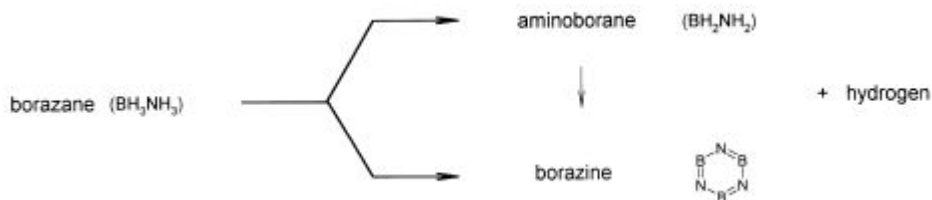


**Figure 2.5.1** The thermal decomposition of borazane under hydrogen release and formation of aminoborane and borazine. [Wolf et al., 2000]

Usually for the decomposition two steps are observed. Both steps of the decomposition and with it of the hydrogen release should be exothermic. This was surprising compared with the well-studied decomposition of metal hydrides.

Over the years, several synthetic procedures have been developed to prepare  $\text{H}_3\text{BNH}_3$ , the preparation costs are still high (~\$10 per gram), borazane is not made commercially in large quantities [Shore 1955][Parry 1958]. This is due to difficulties involved in its preparation and especially in its purification.

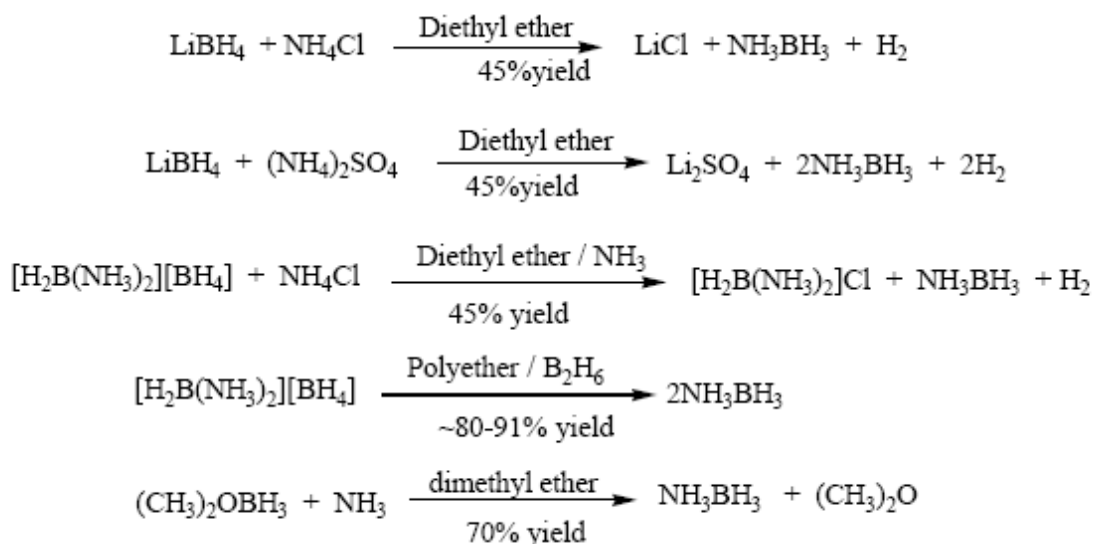


**Figure 2.5.2** synthetic procedures prepare  $\text{H}_3\text{BNH}_3$ , [Shore 1955] [Parry 1958]

### 2.5.1 Modeling of $\text{H}_3\text{BNH}_3$ structure

It is pertinent to summaries relevant aspects of dihydrogen-bonding and related phenomena. A dihydrogen bond can be considered as having two components. These are generally described as ‘donor’ and ‘acceptor’ units (Fig. 2.5.1.2a). Confusion can arise here, however, because ‘donor’ and ‘acceptor’ are used in this dihydrogen-bonding context to describe hydrogen donors and acceptors, and thence have an opposite polar sense to the more commonly encountered concepts of Lewis-base donors and Lewis-acid acceptors.

In the hydrogen-donor units considered here, hydrogen is bonded to a more electronegative element, so that the hydrogen atom is positively polarised. In a conventional hydrogen bond, this would then interact with the lone pair of an electronegative element, i.e. it would donate its positively polarised hydrogen atom to the negatively polarised electronegative element. In dihydrogen-bonding (Fig. 2.5.1.2c), the hydrogen-acceptor unit has its hydrogen atom bonded to a more electropositive element, such as, in the present context, boron. This negatively polarised hydrogen atom is regarded as accepting the positively charged hydrogen atom of the donor unit to form the dihydrogen bond. A positively polarised hydrogen atom can therefore interact attractively with a lone pair to form a conventional hydrogen bond, or with a negatively polarised hydrogen atom, e.g. that of a  $\text{BH}_3$  group, to form a dihydrogen bond. Related to this, a positively polarised hydrogen atom can interact with an electron-rich  $\pi$ -system to form a weakly attractive  $\pi$ -to-hydrogen non-covalent bond (fig. 2.5.1.2b, fig.2.5.1.2d). This last can also be significant in supramolecular assemblies of boron-containing cluster compounds. Of these ‘weaker’ interactions, the BH-HN dihydrogen-bonding interaction is the best examined by Richardson et al. and Kloster et al.. This bonding is typified by close interhydrogen approaches well within van der waals radius sums, with interhydrogen distances well below  $2.0 \text{ \AA}$  being common. There are also specific directional characteristics, with the BHH and NHH angles generally falling into the more acute and more obtuse ranges of  $95^\circ$ – $115^\circ$  and  $150^\circ$ – $170^\circ$ , respectively.

$\text{H}_3\text{BNH}_3$  compound illustrates the dramatic effect of dihydrogen-bonding on physical properties, just like conventional hydrogen-bonding in, for example, with HF and  $\text{H}_2\text{O}$ . The  $\text{H}_3\text{BNH}_3$  molecule is isoelectronic and isostructural, in gas-phase molecular terms, with the ethane molecule,  $\text{H}_3\text{CCCH}_3$ . However,  $\text{H}_3\text{CCCH}_3$  melts at  $-181^\circ\text{C}$ , whereas

$\text{H}_3\text{BNH}_3$  melts nearly  $300^\circ$  higher, at  $+104^\circ\text{C}$ . Although some of this difference arises from the dipole moment of ammonia borane and consequent dipole-dipole attraction, this is probably not a significant contribution. Isoelectronic  $\text{H}_3\text{CF}$ , for example, which is a more polar molecule than  $\text{H}_3\text{BNH}_3$ , melts at  $-142^\circ\text{C}$ . It is currently thought that this higher melting point of  $\text{H}_3\text{BNH}_3$  arises largely from dihydrogen-bonding [Richardson et al.].

The solid-state structure of  $\text{H}_3\text{BNH}_3$  was reported some time ago (Fig. 2.5.1.3, top right) [Kloster et al.]. An analysis of the intermolecular close approaches in the crystalline lattice shows that in an individual  $\text{H}_3\text{BNH}_3$  molecule, every hydrogen atom is involved in dihydrogen-bonding (Fig. 2.5.1.3, top left). Interestingly these are all bifurcated bonds; i.e. one NH donor unit is within dihydrogen-bonding distance of two acceptor BH units. Here we apply the KAP method to the appreciation of the overall dihydrogen-bonding network.

Each  $\text{H}_3\text{BNH}_3$  molecule possesses crystallographic mirror symmetry. One  $\text{H}_3\text{BNH}_3$  molecule can be placed near the origin (Fig. 2.5.1.3, centre right), and a 21 screw chain can thence be developed along the c-axis (Fig. 2.5.1.3, centre left). The series of dihydrogen bonds linking successive molecules is readily apparent. This chain substructure can then be developed into a sheet substructure by a permitted translation along the crystallographic a-axis (Fig. 2.5.1.3, lower). This reveals another set of dihydrogen bonds, now holding the chains together in a sheet.

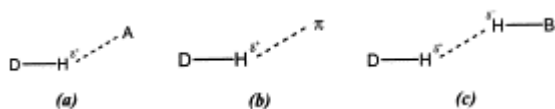


**Figure 2.5.1.1** Schematic representation of: (a) a classical hydrogen bond; (b) a non-classical hydrogen bond; and (c) a ‘dihydrogen’ bond [O’Dowd et al.].

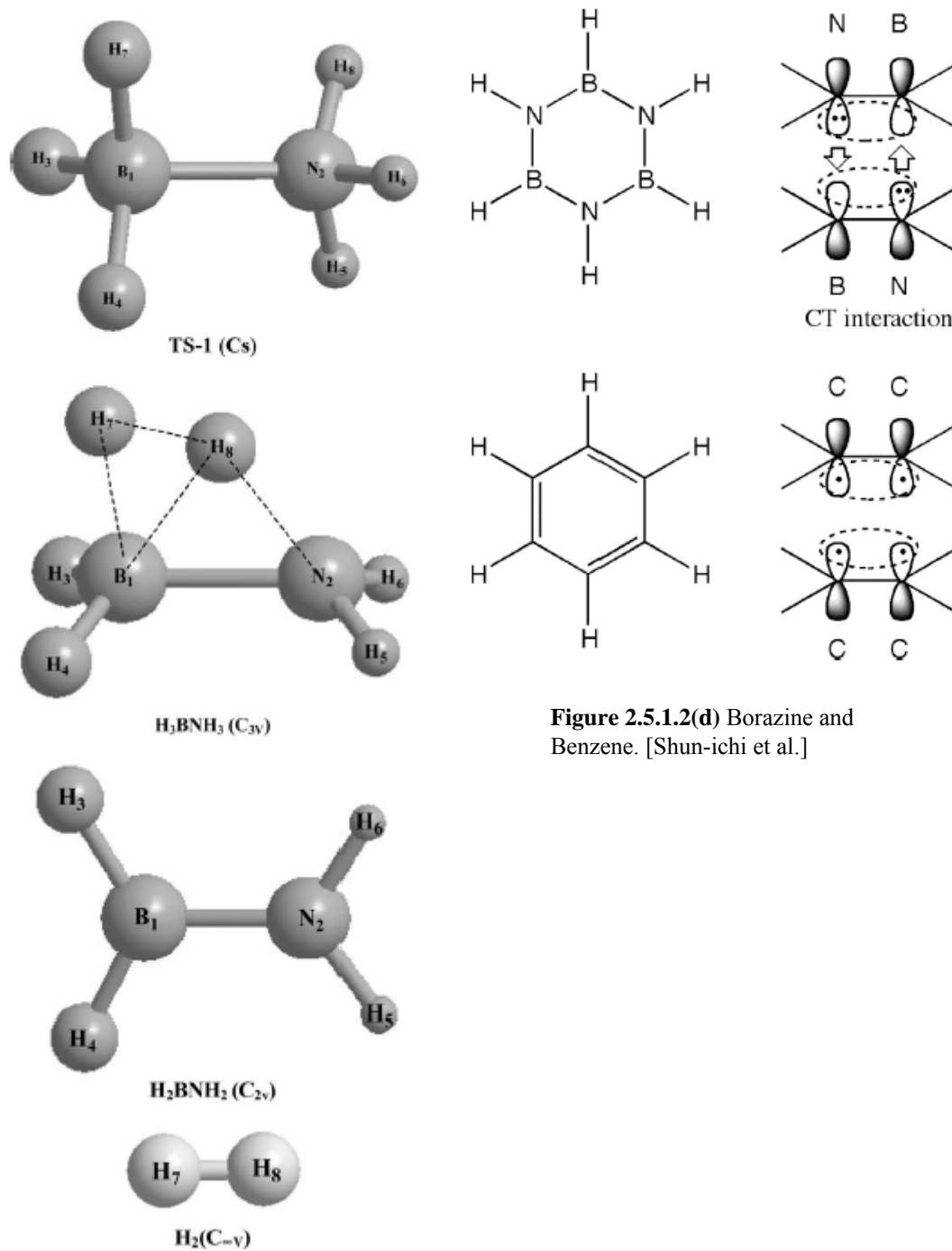
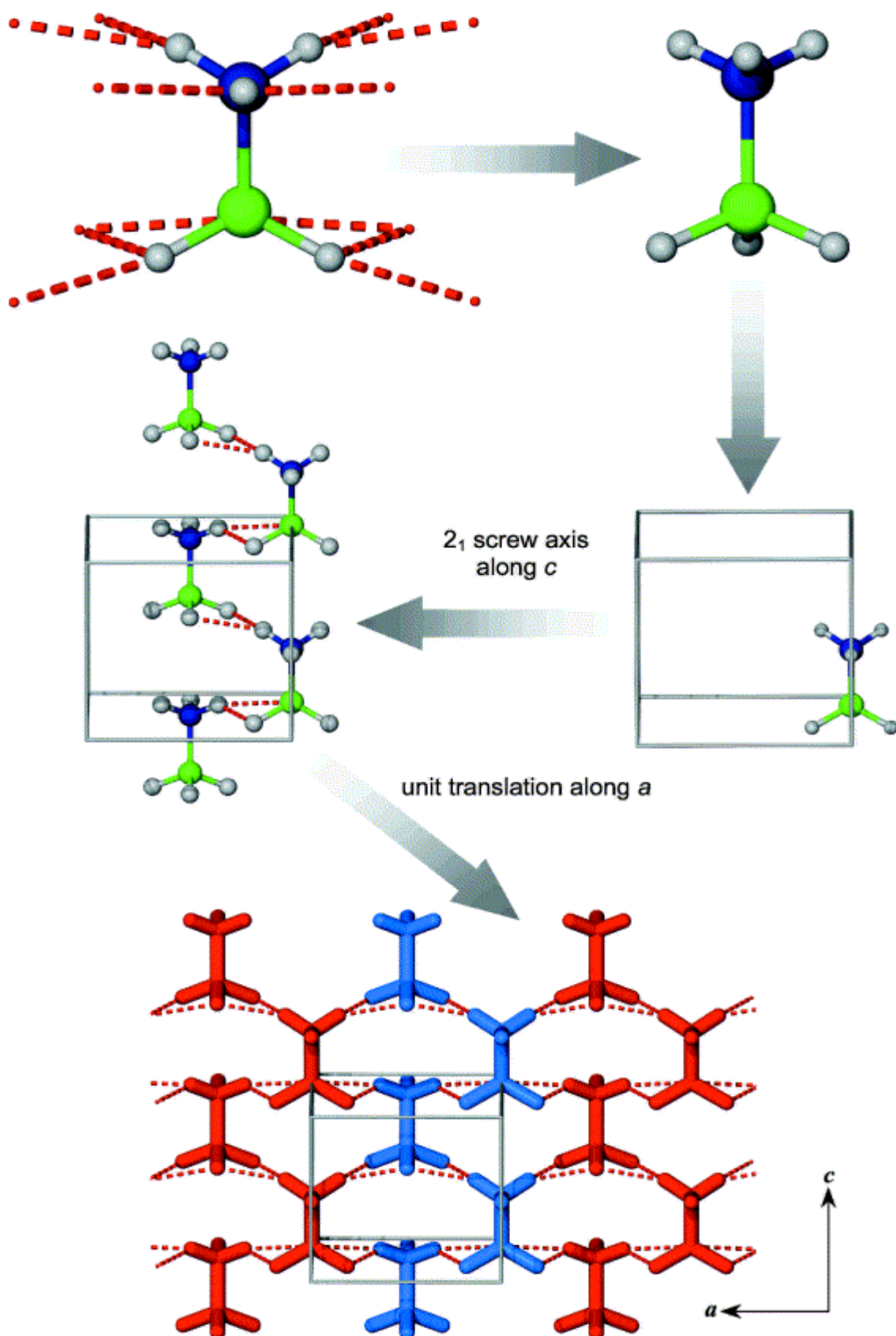
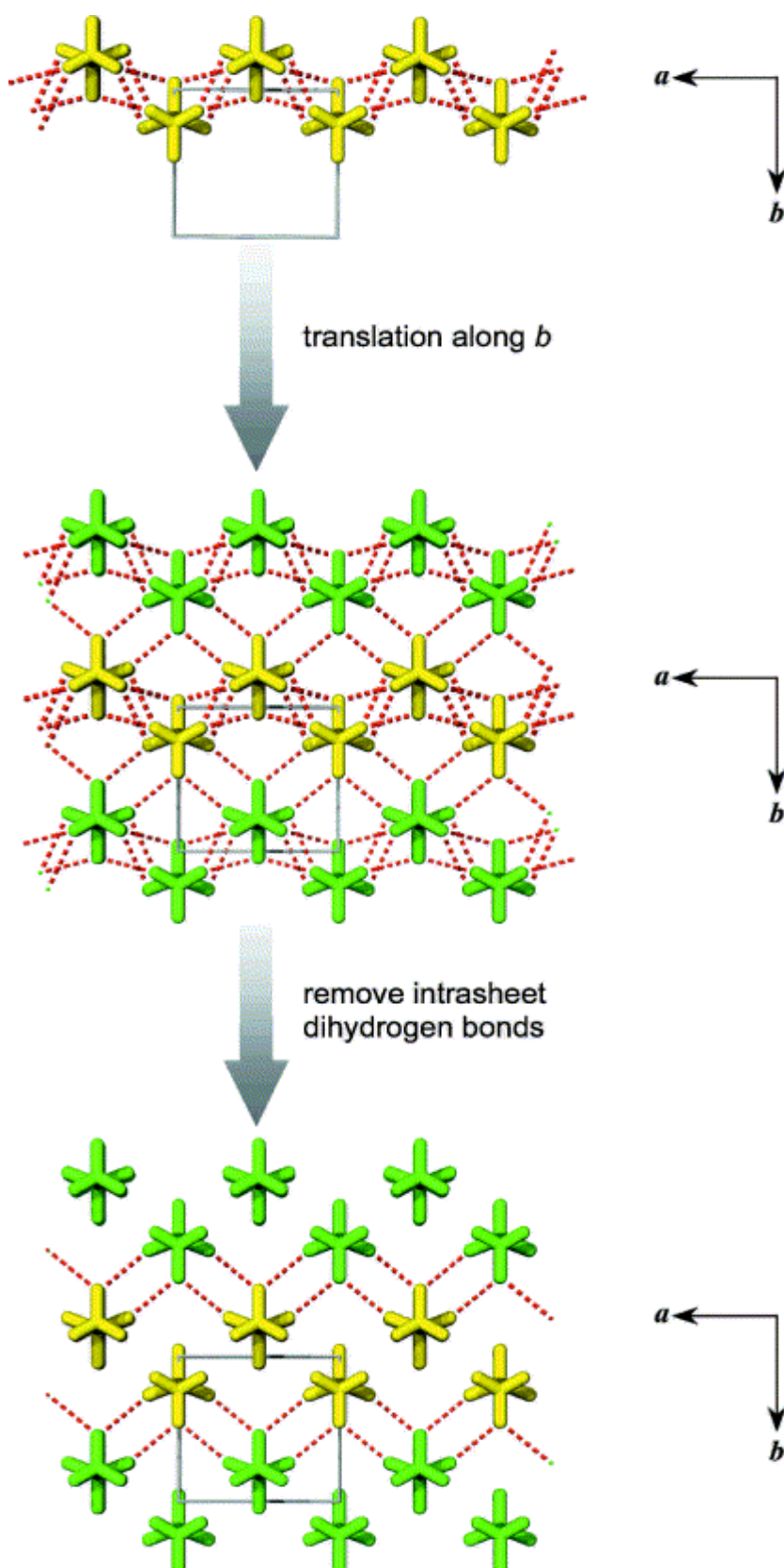


Fig. 2.5.1.2(e) Pictorial of optimised geometries of the stationary points. [Qian et al.]



**Figure 2.5.1.3.** The molecular structure of,  $\text{H}_3\text{NBH}_3$ , with intermolecular dihydrogen bonds included (top left), and omitted (top right), and the first two stages of KAP. The  $2_1$  screw axis along  $c$  at  $a=, b=0$  is used to develop the chain structure (centre left) and successive unit translations along the crystallographic  $a$ -axis thence generate the close-packed sheet (lower diagram). The chain components of sheet structure have been highlighted using alternate red and blue colours [O'Dowd et al.].



**Figure 2.5.1.4.** The sheet substructure generated in Fig. 2.5.1.3, rotated by  $90^\circ$  about the  $a$ -axis (upper diagram), develops into the full three-dimensional structure by applying successive unit translations along the crystallographic  $b$ -axis. The resultant three-dimensional network appears complicated (centre diagram) but is considerably simplified when previously rationalised contacts within the sheet (Fig.2.5.1.2) are omitted (lower diagram). Note that the sheet substructures have been highlighted using alternate yellow and green colours [O'Dowd et al.].

The generation of the macroscopic crystal structure of  $\text{H}_3\text{BNH}_3$  from this KAP sheet is conveniently envisaged via the orthogonal view in the bc plane, looking along the crystallographic b-axis (Fig. 2.5.1.4, upper diagram). The sheet structure develops into the macro structure via successive unit translations along the crystallographic b-axis (Fig. 2.5.1.4, centre). This develops the entire network of dihydrogen bonds that binds the crystal together so effectively. The individual interactions constitute a complex matrix that is difficult to elucidate in diagrams such as this. However, the removal from the diagram of all the dihydrogen bonds associated with the development of the initial chain and sheet substructure readily distinguishes the intersheet dihydrogen bonds (Fig. 2.5.1.4, lower). The KAP methodology therefore nicely enables a clearer analysis and understanding of what at first appears to be a very complicated three-dimensional network of interactions (Fig. 2.5.1.3, upper left). It therefore can give an improved analysis and appreciation beyond that originally presented by Thomas et al. and Kloster et al..

### **2.5.2 Calorimetric process monitoring of thermal decomposition of $\text{H}_3\text{BNH}_3$ compound at Isothermal temperature**

Wolf et al. have worked extensively on  $\text{H}_3\text{BNH}_3$  they have used the techniques of TG/DSC, calorimetry, coupled TG/FTIR, XRD to analyze the basics of  $\text{H}_3\text{BNH}_3$  decomposition reaction in detail. According to the finding and the paper they have published it is clear that borazane can decompose below its melting point. They have worked out that at isothermal temperature of 363K-343K  $\text{H}_3\text{BNH}_3$  decompose completely below its melting point of 393K, as shown in fig. 2.5.2.1. It is clear that at 363K it takes 40minutes to reach the maximum exothermic reaction. But at 343K it takes more than 24 hours to complete the decomposition.

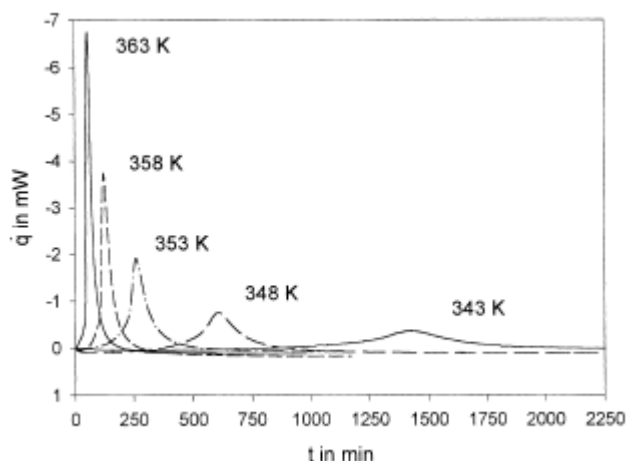


**Figure 2.5.2.1** DSC C 80 curves of thermal decomposition of  $\text{BH}_3\text{NH}_3$ : (—) heating rate 0.05 K/min, (---) heating rate 1 K/min. [Wolf et al. 2000]

They have analyzed the solid residue after the reaction by XRD and FTIR and it is found to be  $(\text{BH}_2\text{NH}_2)_x$  and borazane  $\text{H}_6\text{B}_3\text{N}_3$  Fig. 2.5.1. They analyze hydrogen evolved at isothermal temperature and it was observed that the decomposition under isothermal conditions at temperatures 363K yields approximately 1.0 mol  $\text{H}_2$ /mol  $\text{BH}_3\text{NH}_3$ (fig. 2.5.2.3). Simultaneous TG/DSC measurements are sensitive to the formation of evolved gaseous products. The TG/DSC curves for the isothermal decomposition of borazane at  $T=363\text{ K}$  are shown in (fig. 2.5.2.4), which shows a single significant step of mass loss.

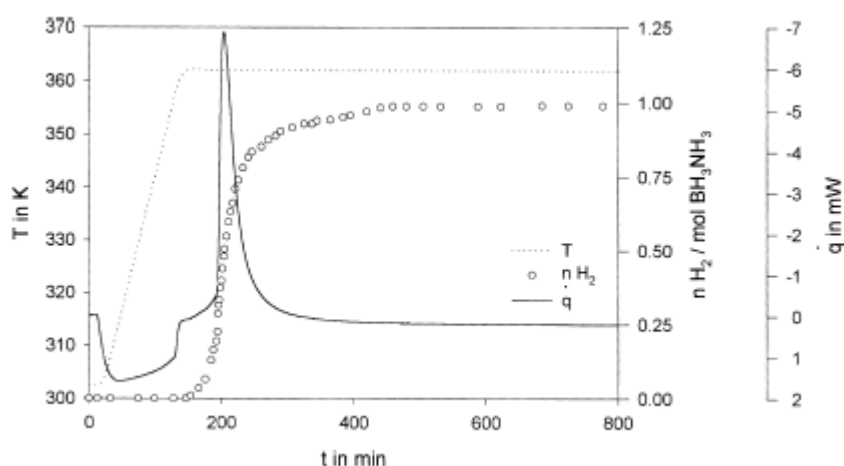


**Figure 2.5.2.2** Volumetric measurement at isothermal temperature 363 K: (—) heat flow, (•••) temperature, (°) evolved hydrogen. [Wolf et al. 2000]

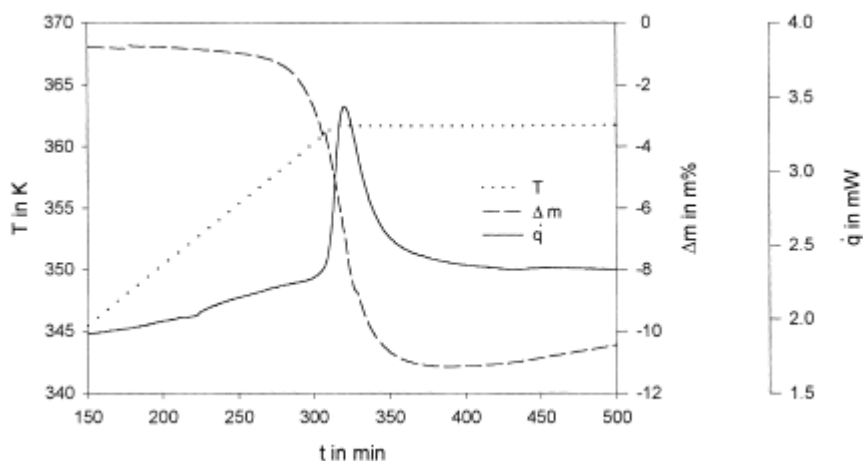


**Figure 2.5.2.3** TG/DSC curves of  $\text{BH}_3\text{NH}_3$  at isothermal temperature 363 K: (—) heat flow, (•••) temperature, (---) mass loss. [Wolf et al. 2000]

Fig. 2.5.2.4 shows TG–FTIR investigations of the decomposition of borazane at 363K, a single significant step of mass loss was detected, slightly beginning at 340K. The final mass loss is about  $\Delta m = (10.2 \pm 0.1)\%$  of the initial sample mass. Monomeric aminoborane  $\text{BH}_2\text{NH}_2$  and borazine  $\text{B}_3\text{N}_3\text{H}_6$  was identified in the evolved gas phase after Comparisons with known spectra data.

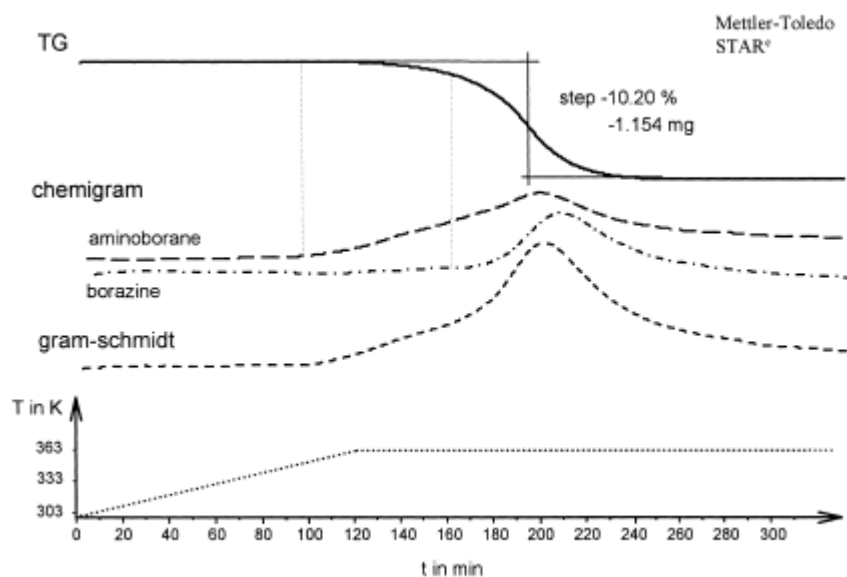


**Figure 2.5.2.4** TG/FTIR-investigations to characterisation of evolved gas phase: (—) mass loss, (•••) temperature, (---) chemigram aminoborane, (- · -) chemigram borazine, (- - -) gram-schmidt. [Wolf et al. 2000]

### 2.5.3 Thermal decomposition of $\text{H}_3\text{BNH}_3$ compounds investigated by using combined thermoanalytical methods

Wolf et al. have also investigated the decomposition reaction of  $\text{H}_3\text{BNH}_3$  at different heating rate and it is shown in fig. 2.5.3.1. At heating rate of 1K/minute two steps were found, first an exothermic reaction starts at 368K and it is then changed into an endothermic reaction which then again change into an exothermic reaction which starts at 378K and has maximum at 382K. It is seen that it is not completely finished and another reaction starts at 400K. Four heating rates of 0.05 K/min they have found that there is no two reaction and that it's only one exothermic reaction that starts at 354K and ends at 364K and has maxima at 360K.

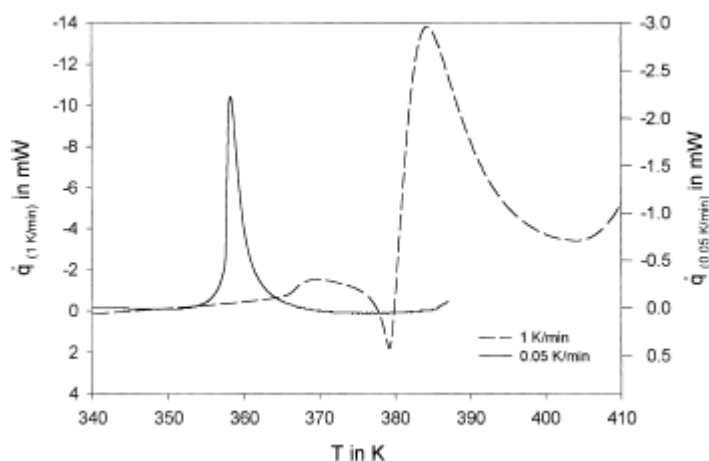


**Fig. 2.5.3.1** DSC C 80 curves of thermal decomposition of  $\text{BH}_3\text{NH}_3$ : (—) heating rate 0.05 K/min, (- - -) heating rate 1 K/min. [Wolf et al. 2000]

Two decomposition steps were reported in fig. 2.5.3.2, which refer to two significant exothermic events, shown by Calorimetric measurements of the thermal decomposition of  $\text{BH}_3\text{NH}_3$  at temperatures up to 473 K with heating rates selected in the range of 1–10  $\text{K min}^{-1}$ . A typical DSC plot with an isothermal part at 363 K, followed by a non-isothermal part with heating rate 0.1  $\text{K min}^{-1}$ , is shown in Fig. 2.5.3.3. Therefore, the initial decomposition of borazane under isothermal conditions allows the clear separation of both decomposition steps.

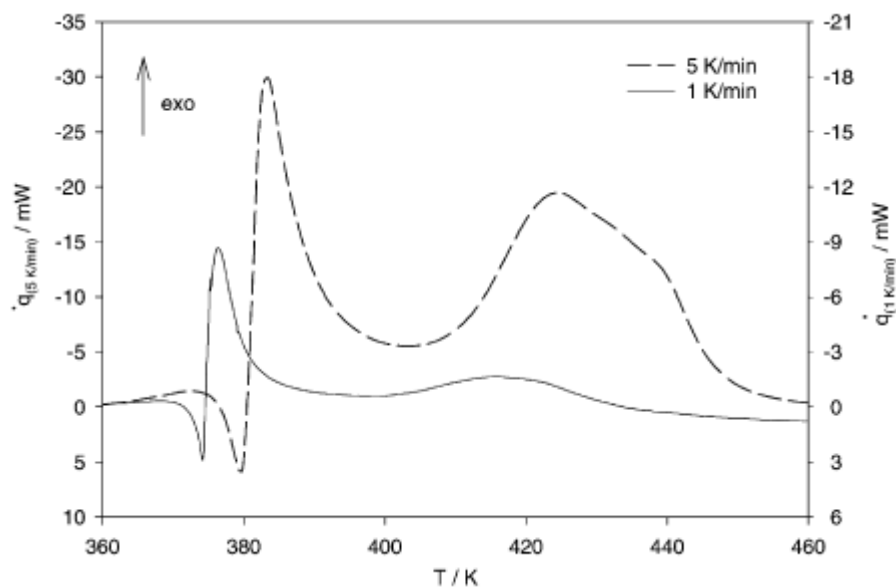


**Fig. 2.5.3.2** Temperature dependence of the heat flow for the thermal decomposition of  $\text{BH}_3\text{NH}_3$  (Setaram DSC 111, argon flow, heating rate  $1 \text{ K min}^{-1}$  (—),  $5 \text{ K min}^{-1}$  (- - -)). [Wolf et al. 2002]

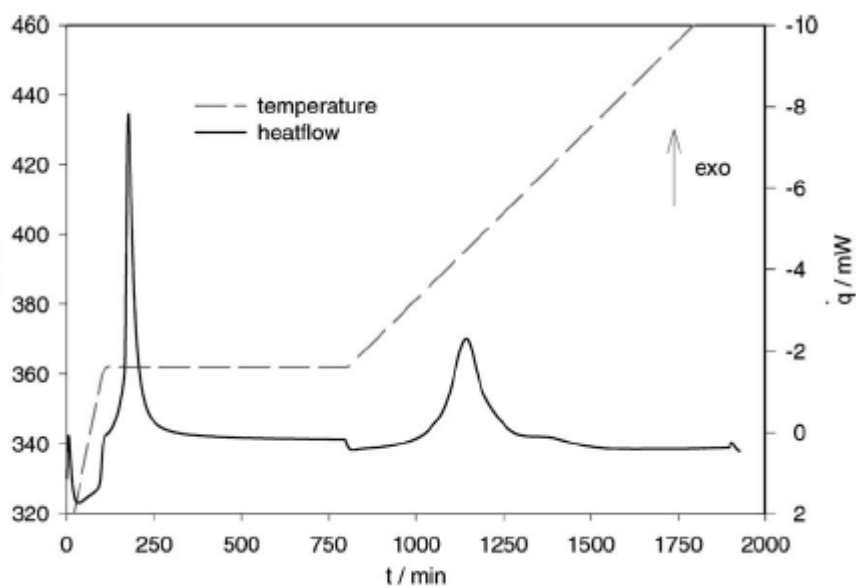


**Fig. 2.5.3.3** Time dependence of the heat flow for the thermal decomposition of  $\text{BH}_3\text{NH}_3$  with an isothermal part at 363 K followed by a non-isothermal part with heating rate  $0.1 \text{ K min}^{-1}$  (Setaram DSC C-80, nitrogen atmosphere). [Wolf et al. 2002]

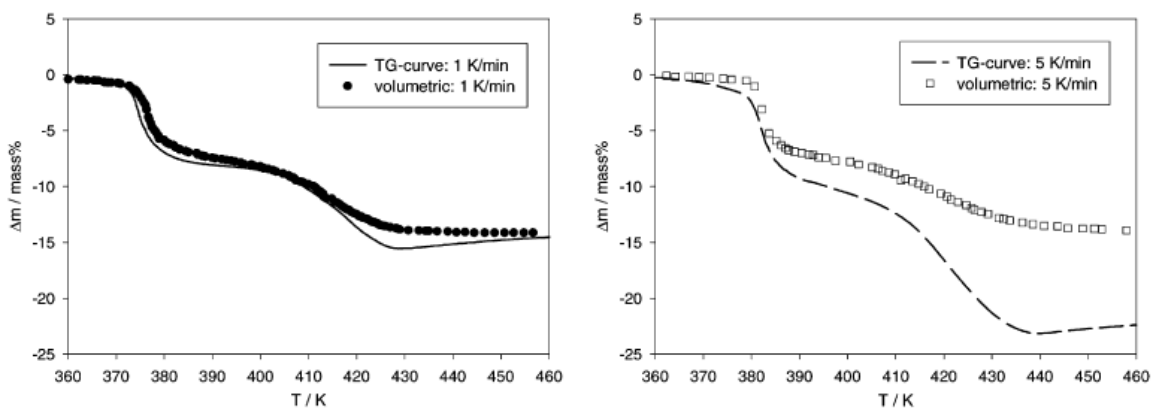


**Fig. 2.5.3.4** Comparison between mass loss data detected thermogravimetrically (line) and calculated from volumetric results (points) (heating rate 1 K min<sup>-1</sup> (a), 5 K min<sup>-1</sup> (b)). [Wolf et al. 2002]

The thermal decomposition of borazane is characterized by two significant steps of mass loss, which correspond to the calorimetrically detected events. Fig. 2.5.3.4 shows the comparison between the detected TG plots and volumetric results converted into mass loss data. During the first step 1.1±0.1 mol H<sub>2</sub>/mol BH<sub>3</sub>NH<sub>3</sub> were released. This value is in good agreement with the proposed formation of polymeric aminoborane (BH<sub>2</sub>NH<sub>2</sub>)<sub>x</sub>. The final value of 2.2±0.1 mol H<sub>2</sub>/mol BH<sub>3</sub>NH<sub>3</sub> was reached at nearly 453 K. The amount of released hydrogen does not increase at higher temperatures and is independent of the used heating rate.

The TG curve in Fig. 2.5.3.5 shows two significant steps of mass loss during the thermal decomposition of borazane in the temperature range up to 513 K performed at heating rate 0.5 K min<sup>-1</sup>. Simultaneous TG/MS analysis was used to establish the means release of gaseous products during the thermal decomposition of borazane in the temperature range up to 473 K, Fig. 2.5.3.6. Detected mass numbers are given in Table 2.5.3.1 and Table 2.5.3.2 together with a possible assignment of the ion peaks. Due to the existence of two natural isotopes for all three elements of borazane, the mass spectra of this compound and all similar compounds are complicated. Table 2.5.3.3 shows the

isotopes natural abundances for B, N, and H elements. It is clear that the two isotopes of boron play an important role in the mass analysis.

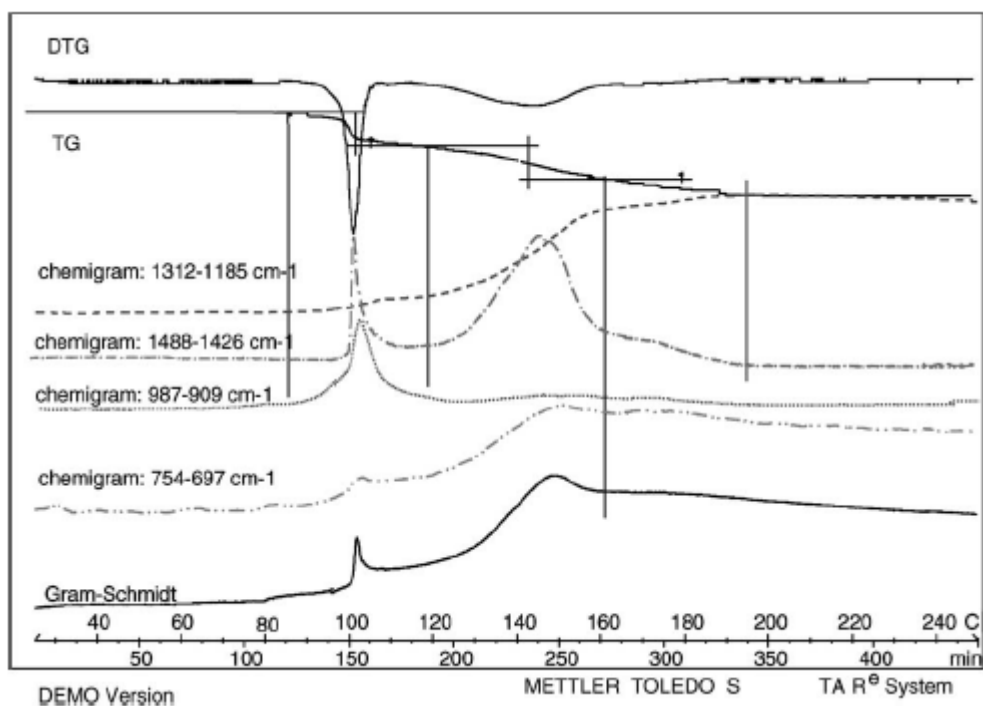


**Figure 2.5.3.5** Simultaneous TG/FTIR analysis of the released gas phase during the thermal decomposition of borazane (heating rate  $0.5 \text{ K min}^{-1}$ ): mass loss, chemigram monomeric aminoborane, chemigram borazine, Gram-Schmidt curve. [Wolf et al. 2002]

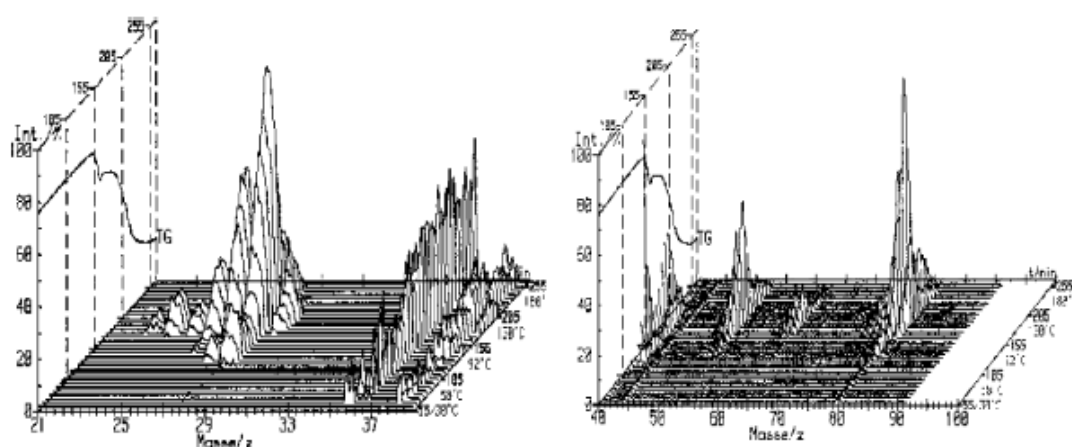


**Figure 2.5.3.6** Simultaneous TG/MS analysis of the released gas phase during the thermal decomposition of borazane (heating rate  $1.5 \text{ K min}^{-1}$ ): mass loss, relative intensity of ion peaks at mass numbers  $m/z$  21– $m/z$  90 [Wolf et al. 2002]

**Table 2.5.3.1** Mass spectrum of the gas phase above  $\text{BH}_3\text{NH}_3$  at elevated temperatures [Wolf et al. 2002]

Mass number	Assignment	Mass number	Assignment
2	$\text{H}_2^+$	27	$^{11}\text{BNH}_2^+, ^{10}\text{BNH}_3^+, ^{11}\text{B}_2\text{H}_5^+$
11	$^{11}\text{B}^+, ^{10}\text{BH}^+$	28	$^{11}\text{BNH}_3^+, ^{10}\text{BNH}_4^+$
12	$^{11}\text{BH}_2^+, ^{10}\text{BH}_2^+$	42	$^{11}\text{BH}_2\text{NH}_2, ^{11}\text{BH}_2^+$
13	$^{11}\text{BH}_2^+, ^{10}\text{BH}_3^+$	53	$^{11}\text{B}_2\text{N}_2\text{H}_3^+$
14	$^{11}\text{BH}_3^+, \text{N}^+$	62	$^{11}\text{B}_3\text{N}_2\text{H}^+$
24	$^{10}\text{BN}^+, ^{11}\text{B}_2\text{H}_2^+, ^{11}\text{B}^{10}\text{BH}_3^+$	63	$^{11}\text{B}_3\text{N}_2\text{H}_2^+$
25	$^{11}\text{BN}^+, ^{10}\text{BNH}^+, ^{11}\text{B}_2\text{H}_3^+$	78	$^{11}\text{B}_3\text{N}_3\text{H}_3^+$
26	$^{11}\text{BNH}^+, ^{10}\text{BNH}_2^+, ^{11}\text{B}_2\text{H}_4^+$	80	$^{11}\text{B}_3\text{N}_3\text{H}_5^+$

**Table 2.5.3.2** Ion mass and tentative identifications for borazine mass spectra. [Nahid et al.]

Mass	Identification
81	$^{11}\text{B}_3\text{N}_3\text{H}_6^+$
80	$^{11}\text{B}_3\text{N}_3\text{H}_5^+, ^{11}\text{B}_2^{10}\text{BN}_3\text{H}_6^+$
79	$^{11}\text{B}_3\text{N}_3\text{H}_4^+, ^{11}\text{B}_2^{10}\text{BN}_3\text{H}_5^+, ^{11}\text{B}^{10}\text{B}_2\text{N}_3\text{H}_6^+$
78	$^{11}\text{B}_3\text{N}_3\text{H}_3^+, ^{11}\text{B}_2^{10}\text{BN}_3\text{H}_4^+, ^{11}\text{B}^{10}\text{B}_2\text{N}_3\text{H}_5^+$
77	$^{11}\text{B}_3\text{N}_3\text{H}_2^+, ^{11}\text{B}_2^{10}\text{BN}_3\text{H}_3^+, ^{11}\text{B}^{10}\text{B}_2\text{N}_3\text{H}_4^+$
76	$^{11}\text{B}_3\text{N}_3\text{H}^+, ^{11}\text{B}_2^{10}\text{BN}_3\text{H}_2^+, ^{11}\text{B}^{10}\text{B}_2\text{N}_3\text{H}_3^+$
75	$^{11}\text{B}_3\text{N}_3^+, ^{11}\text{B}_2^{10}\text{BN}_3\text{H}^+, ^{11}\text{B}^{10}\text{B}_2\text{N}_3\text{H}_2^+$
63	$^{11}\text{B}_3\text{N}_2\text{H}_2^+$
62	$^{11}\text{B}_3\text{N}_2\text{H}^+$
61	$^{11}\text{B}_3\text{N}_2^+$
53	$^{11}\text{B}_2\text{N}_2\text{H}_3^+, ^{11}\text{B}_3\text{NH}_6^+$
52	$^{11}\text{B}_2\text{N}_2\text{H}_2^+, ^{11}\text{B}_3\text{NH}_5^+$
51	$^{11}\text{B}_2\text{N}_2\text{H}^+, ^{11}\text{B}_3\text{NH}_4^+$
39	$^{11}\text{B}_2\text{NH}_3^+$

**Table 2.5.3.3** Natural abundance of B, N and H isotopes. [Nahid et al.]

Element	Mass Number	Natural Abundance
B	10	19.7
	11	80.3
N	14	99.64
	15	0.37
H	1	99.99
	2	0.01